

LARGE-EDDY SIMULATION AND CONJUGATE HEAT TRANSFER IN A ROUND IMPINGING JET

Francis Shum-Kivan, Florent Duchaine*, Laurent Gicquel

CERFACS, 42 avenue G. Coriolis
31 057 Toulouse Cedex 01 France
Email: florent.duchaine@cerfacs.fr

ABSTRACT

This study addresses and evaluates the use of high fidelity Large Eddy Simulation (LES) for the prediction of Conjugate Heat Transfer (CHT) of an impinging jet at a Reynolds number of 23 000, a Mach number of 0.1 and for a nozzle to plate distance of $H/D = 2$. For such simulations mesh point localization as well as the turbulent model and the numerical scheme are known to be of primary importance. In this context, a compressible unstructured third order in time and space LES solver is assessed through the use of WALE sub-grid scale model in a wall-resolved methodology. All simulations discussed in this document well recover main unsteady flow features (the jet core development, the impinging region, the deviation of the flow and the wall jet region) as well as the mean statistics of velocity. Convergence of the wall mesh resolution is investigated by use of 3 meshes and predictions are assessed in terms of wall friction and heat flux. The meshes are based either on full tetrahedral cells or on a hybrid strategy with prism layers at the wall and tetrahedral elsewhere. The hybrid strategy allows reaching good discretization of the boundary layers with a reasonable number of cells. Unsteady flow features retrieved in the jet core, shear layer, impinging region and wall jet region are analyzed and linked to the unsteady and mean heat flux measured at the wall. To finish, a LES based CHT computation relying on the finer grid is used to access the plate temperature distribution. Nusselt number profiles along the plate for the isothermal and the coupled cases are also provided and compared.

NOMENCLATURE

SYMBOLS

D Diameter of the Nozzle jet
 H Nozzle to plate distance
 Nu Nusselt number
 P Pressure
 Pr, Pr_t Prandtl number and turbulent Prandtl number
 q_w Wall heat flux
 r Radius
 Re Reynolds number
 T Temperature
 U_b Bulk velocity
 U_C Centerline velocity
 $r^+, y^+, r\theta^+$ Dimensionless wall distances
 T_j, T_w, T_c Jet, wall and conjugate temperatures
 St_b Strouhal number based on bulk velocity
 λ_s Solid heat conductivity
 λ_t Sub-grid scale turbulent heat conductivity
 ν_t Sub-grid scale turbulent viscosity
 λ_t Sub-grid scale turbulent conductivity
 τ_{wall} Wall friction

ACRONYMS

CFD Computational Fluid Dynamics
CFL Courant Friedrichs Lewy number
CHT Conjugate Heat Transfer
LES Large Eddy Simulation
SGS Sub-Grid Scale

*Address all correspondence to this author.

INTRODUCTION

Determination of heat loads such as wall temperatures and heat fluxes, is a key issue in gas turbine design [1–5]: the interaction of hot gases with colder walls is an important phenomenon and a main design constraint for turbine blades. In recent gas turbines, the constant increase of the thermodynamic efficiency leads to a turbine inlet temperature that is far beyond the materials melting point. As a result, optimized cooling technologies are necessary to ensure life time of the engine without reducing its efficiency. Impinging jets are a common technology to perform efficient localized cooling in aeronautics applications as well as in electronics for example [6–14]. Heat transfer of impinging flows is influenced by various factors like the jet Reynolds number, its exit to wall surface distance, its orifice shape, as well as the surface curvature, roughness, or the free stream turbulence. All these phenomena are individual challenges for efficient and predictive numerical simulations. Among all the currently available numerical methods, Large Eddy Simulations (LES) potentially offer new design paths to diminish development costs of turbines through important reductions of the number of experimental tests. Validation strategies and demonstrations are however still needed for a relevant and routine use of LES on this problem and in a design phase [11, 12, 14–16].

This study addresses and evaluates the use of high fidelity LES for the prediction of Conjugate Heat Transfer (CHT) in an impinging jet at a Reynolds number of 23 000, a Mach number of 0.1 and for a nozzle to plate distance of $H/D = 2$. For such simulations mesh point localization as well as the turbulent model and the numerical scheme are known to be of primary importance. In this context, the capabilities of the unstructured compressible LES solver are assessed through the use of the WALE sub-grid scale model of and wall-resolved methodology. It is showed that all the simulations well recover the main flow features obtained by experimentations: the jet core development, the impinging region and the deviation of the flow and the wall jet region. First and second order statistics of velocity are found to be in good agreement with available experimental and numerical data. Convergence of the wall mesh resolution is investigated by use of 3 meshes and assessed in terms of wall friction and heat flux. The meshes are based either on full tetrahedral cells or on a hybrid strategy with prism layers at the blade wall and tetrahedral elsewhere. The hybrid strategy allows reaching good discretization of the boundary layers (wall unit y^+ close to unity) with a reasonable number of cells. Unsteady flow features retrieved in the jet core, shear layer, impinging region and wall jet region by the LES are then analyzed and linked to the unsteady and mean heat flux measured at the wall. To finish and based on the previous validations, a LES based CHT computation relying on the finer grid is used to access the plate temperature distribution. Nusselt number profiles along the plate for the isothermal and the coupled cases are also provided and compared.

The paper is organized as follows. The target impinging jet

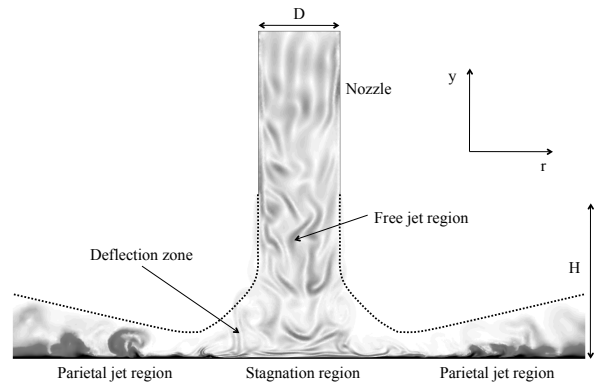


FIGURE 1. Schematic view of the impinging jet configuration.

is first introduced. Then the LES fluid and solid solvers are presented and the numerical setup is detailed. A grid convergence study is achieved and the flow field as well as heat transfer characteristics obtained by the simulations are discussed and compared with experimental data. At this occasion, focus is made on the identification of unsteady flow features controlling the convective heat transfer that LES is able to capture. Finally, a CHT resolution is proposed to gauge the influence on the heat transfer predictions of heat diffusion in the wall.

1 Problem description

The tested configuration is an unconfined 3D turbulent round jet that impinges normally onto a flat plate (Fig. 1). The nozzle to plate distance H is 2 times the diameter D of the jet. The Reynolds number of the jet based on its diameter and bulk velocity is of the order of $Re = 23000$ and the Mach number is 0.1. The case is representative of the experiments of Geers *et al.* [9] and Tummers *et al.* [12] as well as of the numerical simulations of Hadziabdic [10] and Lodato *et al.* [11].

In this range of Reynolds number and nozzle to plate distance, the flow field can be described by 3 main regions (Fig. 1). The first one is the free jet region where the jet is unaffected by the wall. The structure of the flow corresponds to a turbulent free jet without impingement. The axial velocity on the jet axis is almost constant. Due to the short nozzle to wall distance used in this study, the longitudinal size of this region is shorter than typical jet potential core lengths. The second characteristic zone is the impingement region that exhibits a stagnation point as well as a deflexion zone where the axial flow field becomes radial. On the jet axis, the axial velocity decreases until reaching zero at the wall. The third region corresponds to a radial wall jet that develops around the main jet. In this region, viscous forces are dominant and ultimately a turbulent boundary layer develops further downstream along the wall.

Heat transfer at the wall results from this complex flow field

and the nature of turbulence in the stagnation region as well as in the developing wall jet. With the parameters retained for the present study, it is commonly observed that the radial Nusselt number exhibits two peaks [6, 7, 12, 14]: the first one is linked to the stagnation region and impingement of vortical structures on the wall while the second one locates at about $r = 2D$. This latter peak origin is however not clear and there is no consensus on its physical explanation.

This paper proposes the evaluation of a compressible unstructured flow solver based on LES for the prediction of these heat transfer characteristics. Once validated, the solver is used for a CHT computation to gauge the impact of the wall temperature on the thermal flux predictions.

2 Numerical approach

The method adopted to solve the CHT problem in the configuration is to couple a parallel LES solver with a conduction code. Efficient implementation of such a CHT framework requires a software to manage the parallel execution of the two different solvers as well as the data exchanges during their execution. In order to insure the performance of the coupling, a fully parallel code coupler is used [17, 18]. This section describes the fluid and conduction solvers as well as the numerical setup used to model the impinging jet.

Governing equations and LES models.

The initial governing equations solved are the unsteady compressible Navier-Stokes equations that describe the conservation of mass, momentum and energy. For compressible turbulent flows the primary variables are the density ρ , the velocity vector u_i and the total energy $E \equiv e_s + 1/2 u_i u_i$. The fluid follows the ideal gas law, $P = \rho R T$ and $e_s = \int_0^T c_p dT - P/\rho$, where e_s is the sensible energy, P the pressure, T the temperature, c_p the fluid heat capacity at constant pressure and r is the mixture gas constant. The LES solver takes into account changes of heat capacity with temperature using tabulated values of c_p . The viscous stress tensor and the heat diffusion vector use classical gradient approaches. The fluid viscosity follows Sutherland's law and the heat diffusion coefficient follows Fourier's law. The Prandtl number of the fluid is taken as $Pr = 0.72$. The application of the filtering operation to the instantaneous set of compressible Navier-Stokes transport equations yields the LES transport equations [19] which contain Sub-Grid Scale (SGS) quantities that need modelling [20, 21]. The unresolved SGS stress tensor is modelled using the Boussinesq assumption [22, 23]. The Wall Adapting Local Eddy (WALE) model [24] is chosen to model the SGS viscosity. This model is designed to provide correct levels of turbulent viscosity down to the wall and no wall model is required. The SGS energy flux is modeled using a SGS turbulent heat conductivity λ_t obtained from v_t by $\lambda_t = \bar{\rho} v_t c_p / Pr_t$ where the turbulent Prandtl number is kept constant at $Pr_t = 0.5$ [11].

Governing equations for solid heat transfer models.

Heat transfer in solid domains is described by the energy conservation:

$$\rho_s C_s \frac{\partial T(\mathbf{x}, t)}{\partial t} = -\frac{\partial q_i}{\partial x_i} \quad (1)$$

where T is the temperature, ρ_s is the density, C_s is the heat capacity and q the conduction heat flux. The heat diffusion follows Fourier's law $q_i = -\lambda_s \frac{\partial T}{\partial x_i}$ where λ_s is the heat conductivity of the medium. The solid solver takes into account local changes of heat capacity and conductivity with temperature through a tabulation of the material properties.

Numerical schemes.

The parallel LES code [25] solves the full compressible Navier-Stokes equations using a two-step time-explicit Taylor-Galerkin scheme (TTGC or TTG4A) for the hyperbolic terms based on a cell-vertex formulation [26, 27], a second order Galerkin scheme for diffusion [28]. The schemes provide high spectral resolution as well as low numerical dissipation and dispersion. Such numerics are especially designed for LES on hybrid meshes and have been extensively validated in the context of turbulent flow applications [16, 29, 30]. The schemes provides third-order accuracy in space and third-order (TTGC) or fourth-order (TTG4A) accuracy in time [27]. The main difference between TTGC and TTGA4 is linked to the amplification factors of the schemes that show a different behavior on small spatial wave length structures: TTG4A has a more dissipative behavior on small wave lengths compared to TTGC. Nevertheless, TTG4A is less prone to numerical instabilities issued by the centered spatial discretisation. The major drawback of this strategy arises from the explicit nature of the solver whose time step is controlled by the low acoustic CFL number (0.7 for the present computations) preventing from reducing the characteristic cell size below the wall unit scale. Therefore, for aerodynamic applications, where the viscous sub-layer needs to be computed, mesh refinements force small time steps and a higher computational cost is inferred when compared to incompressible code for example. For the most refined mesh M3 (Tab. 1), about 8320 CPU hours are necessary to simulate one flow-through time on 128 cores on a BULL Sandy Bridge machine. Note that despite this clear constraint, the unstructured hybrid approach enables refinement of the mesh in zones of interest by using prisms in the wall region [31, 32].

The parallel conduction solver is based on the same data structure and thus uses a second order Galerkin diffusion scheme [28]. Time integration is done with an implicit first order forward Euler scheme. The resolution of the implicit system is done with a parallel matrix free conjugate gradient method [33].

Computational setup.

The fluid domain is composed of a cylindrical nozzle of diameter D and length $2D$ connected to a cylinder of diameter $7D$ and height $H = 2D$ (Fig. 2). In this paper, the axis of the jet as well as the wall normal direction of the impinged plate are aligned with the y direction. The velocity profile imposed at the inlet of the nozzle is given by [11]:

$$\frac{U(r)}{U_C} = \left(1 - \frac{2r}{D}\right)^{1/7.23} \quad (2)$$

where r is the radial position, and the centerline velocity $U_C = U(r = 0)$ is obtained from the experimental correlation [34]:

$$\frac{U_b}{U_C} = 0.811 + 0.038[\log(Re) - 4] \quad (3)$$

It is important to underline that a fully developed turbulent pipe flow profile exhibits a velocity deficit of about 20% compared to the profile imposed here. Such difference largely impact the development of the jet. The velocity profile associated with a constant temperature are imposed at the inlet of the fluid domain using the Navier-Stokes Characteristic Boundary Condition (NSCBC) formalism [35]. In order to mimic the turbulent flow developing in the nozzle at a Reynolds number of $Re = 23000$, isotropic velocity fluctuations are injected at the inlet following a non reflecting formalism to avoid numerical noise [36]. The simulated jet is unconfined, meaning that the upper boundary of the domain is not a wall but an open boundary. In order to help the stability of the computation, an inlet with a target velocity of the order of 5% of the jet bulk velocity U_b is imposed. Tests from 2% to 10% have been carried out to ensure that the retained co-flow velocity has no influence on the jet impingement region and is sufficient to fill correctly the computational domain. Existing studies show that such moderate co-flow velocity does not impact the impingement region [10]. Static pressure is enforced at the cylindrical outlet boundary in characteristic NSCBC form accounting for transverses terms [37]. The nozzle wall is treated as an adiabatic no slip wall. The plate is treated as an adiabatic no slip wall for the aerodynamic study and as an isothermal no slip wall when heat transfer is considered. In the following, all the quantities are normalized by the jet diameter D and its bulk velocity U_b .

Typical unstructured meshes of complex geometries consist in tetrahedra. In order to provide the right viscous stress and heat flux at the wall, the grid cells adjacent to the wall must be inside the viscous sublayer. This condition requires a high density of very small grid cells close to the wall that leads to expensive simulations. When the boundary layer is explicitly resolved, using prismatic layers close to wall surfaces is more efficient than using tetrahedra. First, quadrilateral faces normal

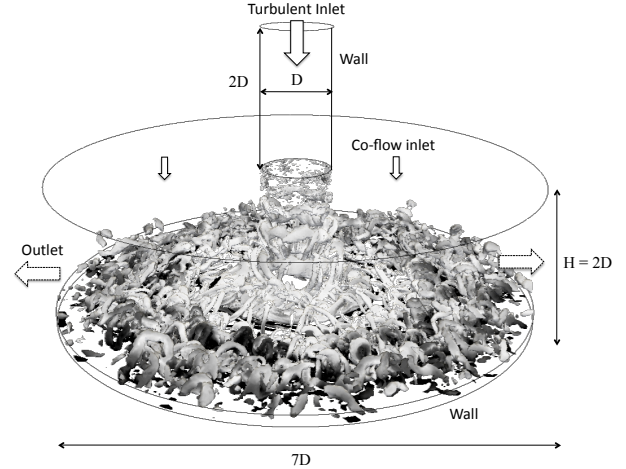


FIGURE 2. Schematic view of computational setup.

to the wall provide good orthogonality and grid-clustering capabilities that are well suited to thin boundary layers, whereas the triangulation in the tangential direction allows for more flexibility in surface modeling. Second, for the same spatial resolution in the normal direction, the prismatic layer approach uses less elements and leads to a higher minimum cell volume than the full tetrahedral grid approach because prismatic elements can have larger aspect ratios. To confirm hybrid mesh capabilities, an approach with prismatic layers in the near-wall region of the impinged plate and tetrahedra in the fluid domain is compared to a full tetrahedra approach [16, 32]. The objective is threefold: (1) reduce the number of cells in the nearby region of the wall, (2) meet the preferential directions of the boundary layer flow and (3) limit the constraint on the acoustic time step. The solution adopted has ten layers of prisms where the vertical length of the prism Δy is smaller than the triangle base-length Δr or $r\Delta\theta$ (here, $\Delta r \approx r\Delta\theta$). The stretching ratio between two prism layer is 1.02. A limit is imposed to this mesh adaptation to avoid numerical errors in these layers: the aspect ratio of the first and thinnest layer is set to $\Delta r \approx r\Delta\theta \approx \alpha\Delta y$, with α lower than 8 (i.e., $r^+ \approx r\theta^+ \approx \alpha y^+$) in agreement with known observations and boundary layer scales [20]. The TTG4A scheme is preferred when using hybrid meshes to ensure a better numerical stability of the simulations.

A mesh dependency study of the mean flow quantities as well as wall friction and heat flux have been done based on three meshes. Due to the flow topology described on Fig. 2, the main regions of importance for proper evaluation of the heat transfer at the wall are:

1. the free jet development region where injected turbulence and shear layer instabilities have to be captured,
2. the deflection region where the flow and turbulent structures

- are reoriented,
3. the wall jet zone where turbulent boundary layers develop,
 4. the impinging wall where the friction and heat transfer take place.

Table 1 gives the main properties of the three meshes. Mesh #1 is a basic pure tetrahedral mesh with attention given to the main jet region. Mesh #2 is obtained from mesh #1 by largely increasing the mesh resolution at the wall in conjunction with a slight decrease of the mesh density in the main jet zone. Finally, mesh #3 takes advantage of hybrid tetrahedral / prism cells to provide a grid with almost the same number of cells mesh #2 but with a higher density in the main jet regions (free jet, deflection) as well as at the wall. Figure 3 shows the evolution of the wall resolution through the radial profiles of normalized wall distance y^+ for the three meshes. As expected, increasing the mesh size leads to a decrease of the measured y^+ . The benefits of the hybrid mesh strategy adopted for mesh #3 is clearly evidenced Tab. 1 leading to y^+ always smaller than 5 in the region of interest without increasing too much the mesh size as compared to mesh #2.

	M1	M2	M3
Number of grid cells	5M	19M	21M
Number of prisms	-	-	4M
Jet cell size [-]	$2 \cdot 10^{-2}$	$4 \cdot 10^{-2}$	$2.25 \cdot 10^{-2}$
Wall cell size [-]	$2 \cdot 10^{-2}$	$6 \cdot 10^{-3}$	$2 \cdot 10^{-3}$
Max cell size [-]	$1 \cdot 10^{-1}$	$1 \cdot 10^{-1}$	$7 \cdot 10^{-2}$
Time step [-]	$3.4 \cdot 10^{-4}$	$7.82 \cdot 10^{-5}$	$1.05 \cdot 10^{-4}$
y^+ [-]	7 - 40	5 - 10	2 - 5
$r^+ \approx r\theta^+$ [-]	7 - 40	5 - 10	8 - 40
Numerical Scheme	TTGC	TTGC	TTG4A
CPU time per τ [hours]	580	8320	8320
Phys. time for stats	4.5τ	1τ	1τ

TABLE 1. Description of the three meshes used. The physical reference time $\tau = V/Q = 22$ [-] correspond to one convective time with V the volume of the domain and Q the mass flow rate.

3 Flow analysis

In this section, the main flow features captured by the LES are analyzed with the results obtained on mesh #3. The grid dependency from mesh #1 to #3 is then assessed based on the

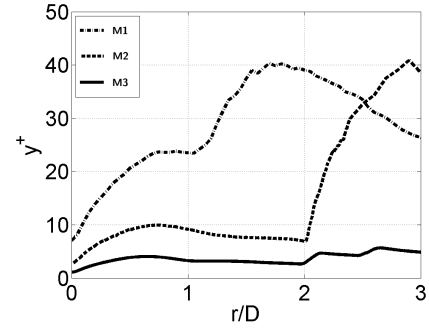


FIGURE 3. Radial profiles of y^+ for the three meshes.

proper resolution of the principal flow characteristics. For the computations presented in this section, the wall is treated as adiabatic.

Description of flow topology.

All the three meshes used in this study retrieve the main instantaneous flow topologies. Figure 4 shows the complex dynamics of the wall jet interaction obtained with mesh #3: the jet shear layer (A), the growth of Kelvin Helmholtz type instabilities leading to ring vortex apparition that experience azimuthal instabilities as well as vortex pairing (B), the generation of elongated vortex structures (C) and finally the transition to a turbulent flow due to the interaction of these structures with the mean flow. The wall shear stress representation on Fig. 4 clearly shows the pattern of the wavy toroidal vortices that hit the wall (B'), the effect of elongated structures on the radial direction (C') as well as the turbulent mixing occurring in the wall jet. The identification of all these structures shows that LES gives a large temporal and spatial spectra of frequencies. The jet vortex ring is the main flow structure. The frequency of its formation obtained by signal analysis and flow visualization corresponds to a Strouhal number St_b based on the bulk velocity U_b and the jet diameter D of the order of $St_b = 1$. Due to the jet deviation and the modification of the local convective velocity along the flow path as well as the different mechanisms of vortex pairing and turbulent generation, the Strouhal number of the vortex wall interaction is about $0.63St_b$. Figure 5 gives the space-time evolution of the vortex dynamics in the mid-plane of the configuration thanks to an iso-surface of the Q-criterion [38]. This 3D view allows to clearly track vortices in space and time: the periodic vortex ring formation in the jet shear layer at $St_b = 1$ followed by the deflection of the flow and the complex interaction between the vortex rings leading to the development of turbulent structures in the wall jet region at about $r/D = 1 - 1.5$.

Mean flow properties.

Mean quantities described in the following of the paper are time and azimuthally averaged. Figure 6 compares the mean ra-

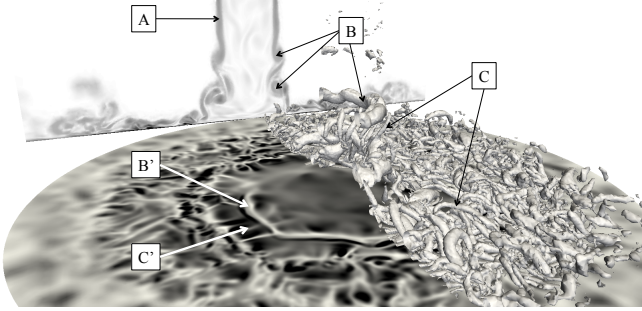


FIGURE 4. Identification of the main flow features responsible for heat transfer. Visualization of vorticity field on the vertical plane, wall shear stress on the plate and iso surface of Q-criterion.

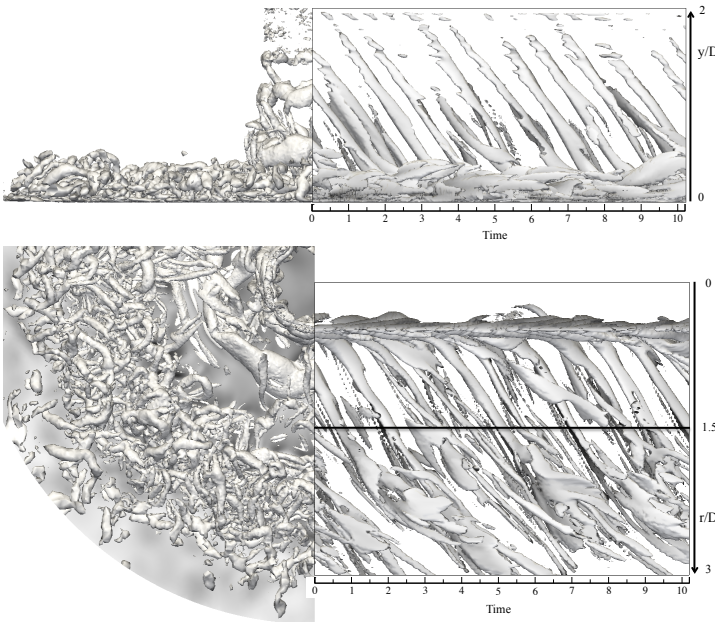


FIGURE 5. Ring vortices traveling in the space-time domain. Left side, instantaneous iso-surface of Q-criterion, left side space-time evolution on half of the jet mid-plane - upper : side view, lower upper view. Time is normalized by D/U_b .

dial and longitudinal velocity profiles along the axial direction y obtained with the three meshes with experimental data [9, 12]. The simulations with the three meshes reproduce accurately the radial and longitudinal profiles at different radial positions. Mesh resolutions inside the domain (comparing M1 with M2) or at the wall (comparing M1 with M3) are sufficient to capture the mean flow properties inside the different jet regions. The mean axial flow property is well captured as evidenced by the null radial velocity on the jet axis ($r/D = 0$). The potential core of the free jet

is illustrated on Fig. 6-d with a plateau of axial velocity on the jet axis, which start to drastically decrease at $y/D = 0.9$ when approaching the wall. This decrease linked to the radial flow redirection is accompanied with the wall jet generation that accelerates along the wall: the peak of radial velocity is about $0.8 U_b$ at $r/D = 0.5$ (Fig. 6-b) and then $1.15 U_b$ at $r/D = 1$ (Fig. 6-c).

The axial distributions of fluctuating velocities $u'_r u'_r$ and $u'_v u'_v$ are presented on Fig. 7. The shape of the profiles are globally well captured. Nevertheless, the simulations have the tendency to over-predict the levels in a large part of the domain above $y/D = 0.2$ (mainly with mesh #3). Compared to existing LES on structured grids [10, 11, 14], present fluctuating velocity results exhibit poorer quality. Explanations can be linked to the important backscatter from small turbulent scales to bigger ones that takes place in such configurations and which is not taken into account in the SGS model used, as evidenced by Lodato *et al.* [11]. A related reason probably responsible for the high level of velocity fluctuations in the shear layer of the free jet (Fig. 7-b) as well as in the shear layer of the wall jet (Fig. 7-f) is the too coherent prediction of turbulent structures that contain a lot of energy and a long lifetime indicating of a potential too low effective Reynolds number in parts of the flow. This can be either linked to the mesh quality as well as in the turbulent length scales injected at the inlet.

The radial wall friction distributions resulting from the three computations compared to measurements [12] are plotted on Fig. 8. The profiles illustrate the convergence of the wall shear when increasing the wall resolution. Only mesh #3 exhibits the right trend of the curve as well the levels of friction intensity. In the core of the jet (from $r/D = 0$ to 0.5), the wall friction increases due to the acceleration of the flow along the plate. A maximum of shear stress is observed next to $r/D = 0.5$ where the vortex rings impact the wall and the flow continues to accelerate significantly. This acceleration of the wall jet continues until about $r/D = 1$ as evidenced on Fig. 6 and 9 and then reaches an almost established convective velocity. From $r/D = 1$ to 1.5 , the wall friction distribution shows a plateau which is related to the intense interaction between vortex rings and local turbulent structures mentioned previously and illustrated by a peak of pressure fluctuations (Fig. 9). This region of intense flow activity has been reported in many works under different point of views and is responsible for the second peak of heat transfer [6, 7, 12, 14]. Finally from $r/D = 1.5$ to the end of the region of interest, a turbulent boundary layer develops along the wall with a slight continuous decrease of the convective velocity due to the expansion of the flow passage surface. I results a continuous decrease of the wall friction after $r/D = 1.5$ (Fig. 8).

4 Heat transfer analysis

The previous section has described the main aerodynamic features captured by LES both in terms of unsteady phenomenon

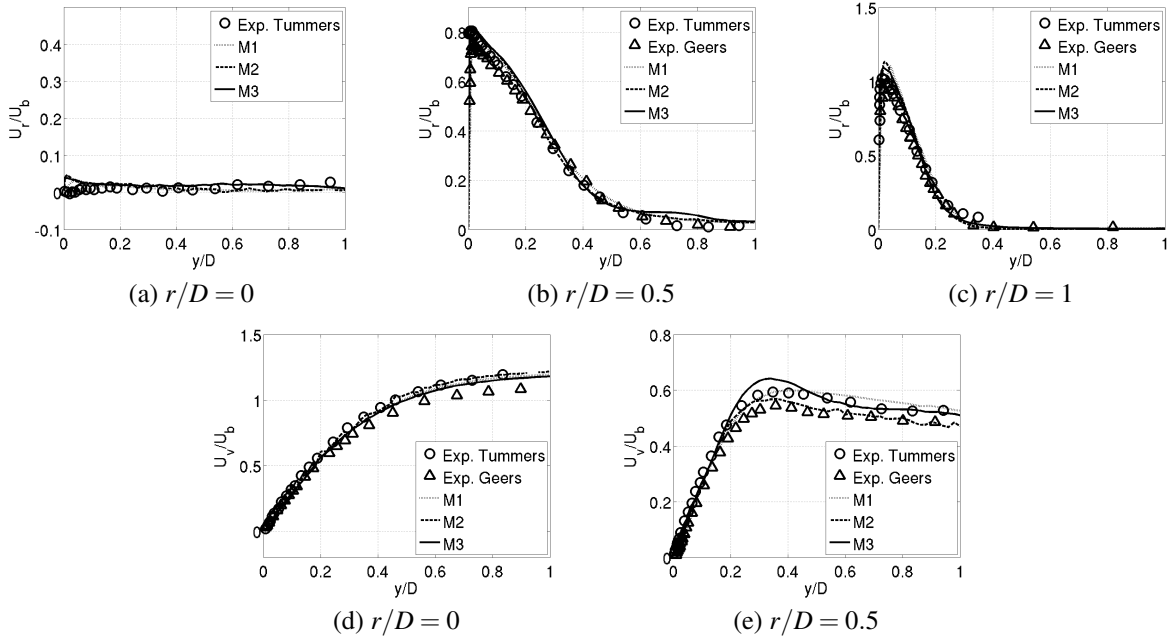


FIGURE 6. Axial profiles of radial velocity (up) and axial velocity (down) for different radial positions.

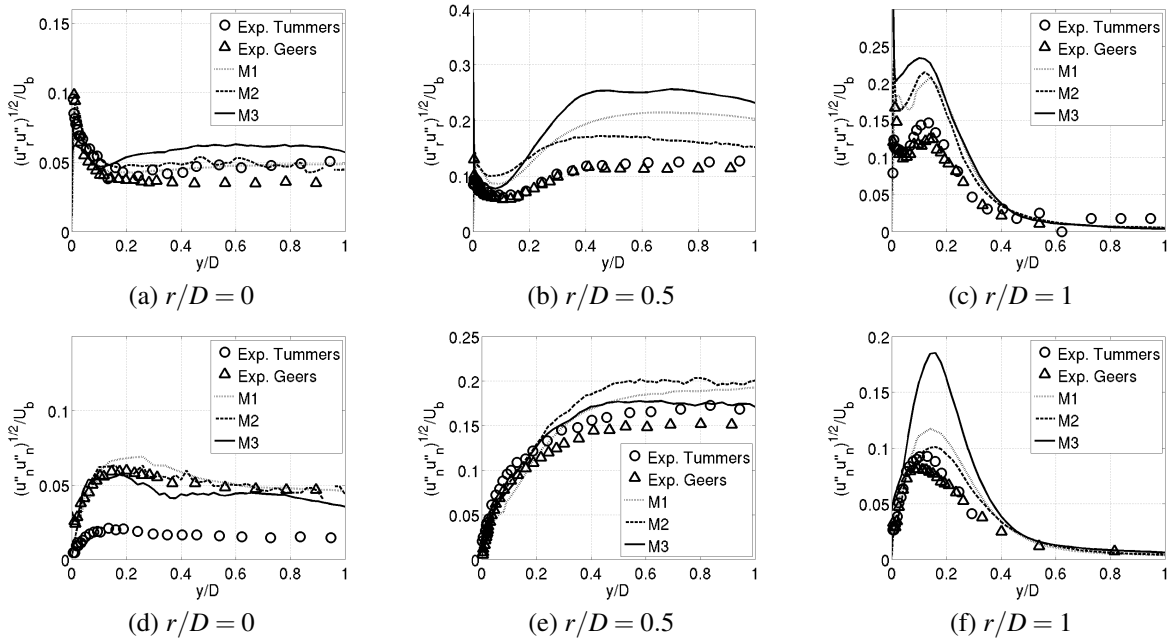


FIGURE 7. Axial profiles of radial velocity fluctuations (up) and axial velocity fluctuations (down) for different radial positions.

and mean compartments. This section is devoted to the heat transfer study between the jet and the wall. To do so, the impinged wall is treated either as an isothermal no slip condition with a fixed temperature $T_w = 1.1T_j$, T_j being the inlet jet tem-

perature, or as an isothermal no slip condition with a temperature T_c issuing from a conjugate heat transfer computation. When CHT is used, the solid domain consists in a cylinder with a radius equal to $3.5D$ and a thickness of $0.1D$ with the outer wall

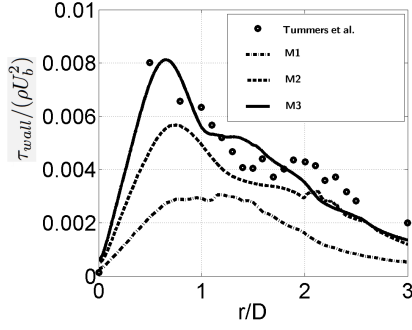


FIGURE 8. Radial wall friction distribution.

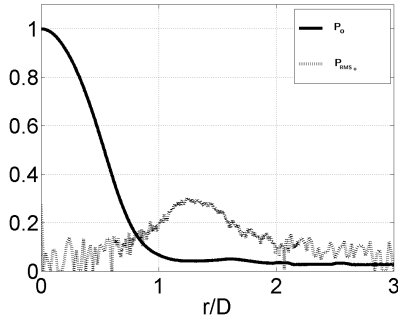


FIGURE 9. Radial wall mean and fluctuating normalized pressure distributions.

temperature imposed to T_w . Small temperature differences are used to avoid buoyancy effects as well as to keep fluid heat conductivity and capacity constant. The thermal conductivity of the solid is $\lambda_s = 38.8\lambda_f$ where λ_f is the fluid conductivity. Details about the CHT methodologies with LES are provided in [16].

Figure 12 shows the radial distribution of the Nusselt number on the impinged wall for the three isothermal simulations performed with mesh #1 to #3 and the coupled simulation done with mesh #3 compared to experimental data [39]. The convergence of the Nusselt number profiles towards experimental data as the wall mesh refinement increases is clearly identified. The resolution of mesh #1 is too poor to capture the shape and level of the profile, whereas the simulation with mesh #2 gives a distribution of heat transfer coherent with experimental data in terms of shape but underestimates a lot the levels. Results obtained with the third mesh are the most accurate. Interestingly, existing LES results on structured grids with better wall resolution than current simulations [10, 14] give better estimations of the Nusselt number profile. In the setup condition ($Re = 23000$ and $H/D = 2$), both experimental and results with mesh #3 exhibit a peak of Nusselt number at the stagnation point ($r/D = 0$). The Nusselt number is then almost constant in the jet core until the impingement

of the vortex rings ($r/D = 0.6$). In the simulation, convective heat transfer decreases deeply until about $r/D = 1$ corresponding to beginning of the intense mixing zone described in the previous section. This important flow activity is the starting point of the second Nusselt number peak whose maximum locates at $r/D = 1.6$ in the present simulation. The Nusselt number peak of experimental results are generally centered around $r/D = 2$ [14], showing modelization weaknesses of both the aerodynamic and the heat transfer at the wall. Investigations have to be done to clarify the interactions between the mesh, the numerical schemes as well as the SGS models in the unsteady flow field predictions and the impact on the heat flux results. To do so, the dynamic in the fluid domain has to be related to wall quantities such as friction and heat flux through advanced analyses, necessary to identify the role of the mean flow and of unsteady motions on the 4 main flow regimes in the near wall region evidenced previously: (1) $0 \leq r/D \leq 0.6$ where the shear stress increases while the heat flux decreases, (2) $0.6 \leq r/D \leq 1$ where both the shear stress and heat flux decrease, (3) $1 \leq r/D \leq 1.5$ with an increase of heat flux and a decrease of the shear stress, and finally $1.5 \leq r/D$ where both quantities decrease. For example, Fig. 10 presents the probability density functions (PDFs) of Nusselt number time series at 7 stations along a radius of the configurations. The shape of the PDFs illustrates the flow regime that develops along the wall, going from a Gaussian with small standard deviation at the center of the configuration to a log-normale like PDF with significant spreading around $r/D = 1$ where turbulence starts to fully develop due to ring vortex interactions. To extract the part of the fluid activity that creates shear stress and heat flux at the wall at the main flow frequency, the local power spectral density at the Strouhal number $0.63St_b$ is performed on a temporal set of fluid solutions. Temporal contribution of shear stress and Nusselt number at $St = 0.63St_b$ are thus decomposed as followed:

$$\begin{aligned}\tau_{wall}^{St}(t) &= \overline{\tau_{wall}^{St}} + (\tau_{wall}^{St})' = \overline{\tau_{wall}^{St}} + A_{\tau} \sin(\omega t + \phi_{\tau}) \\ Nu^{St}(t) &= \overline{Nu^{St}} + (Nu^{St})' = \overline{Nu^{St}} + A_{Nu} \sin(\omega t + \phi_{Nu})\end{aligned}\quad (4)$$

where ω is pulsation associated to the Strouhal number. Figure 11 illustrates the correlations between the fluctuating wall shear stress and heat flux as well as the convective nature of the fluctuating parts $(\tau_{wall}^{St})'$ and $(Nu^{St})'$. The fluctuations of the wall variables at this Strouhal number of $0.63St_b$ represent an important percentage of the mean profiles (up to 20% for the friction and 10% for the heat flux). Note also that the 4 main flow regions are visible on the profiles which illustrates the contribution of these structures on wall quantities at this particular frequency.

To conclude, coupled and isothermal simulations give almost the same distribution of Nusselt number along the wall (Fig. 12), i.e. in these conditions the heat transfer coefficient

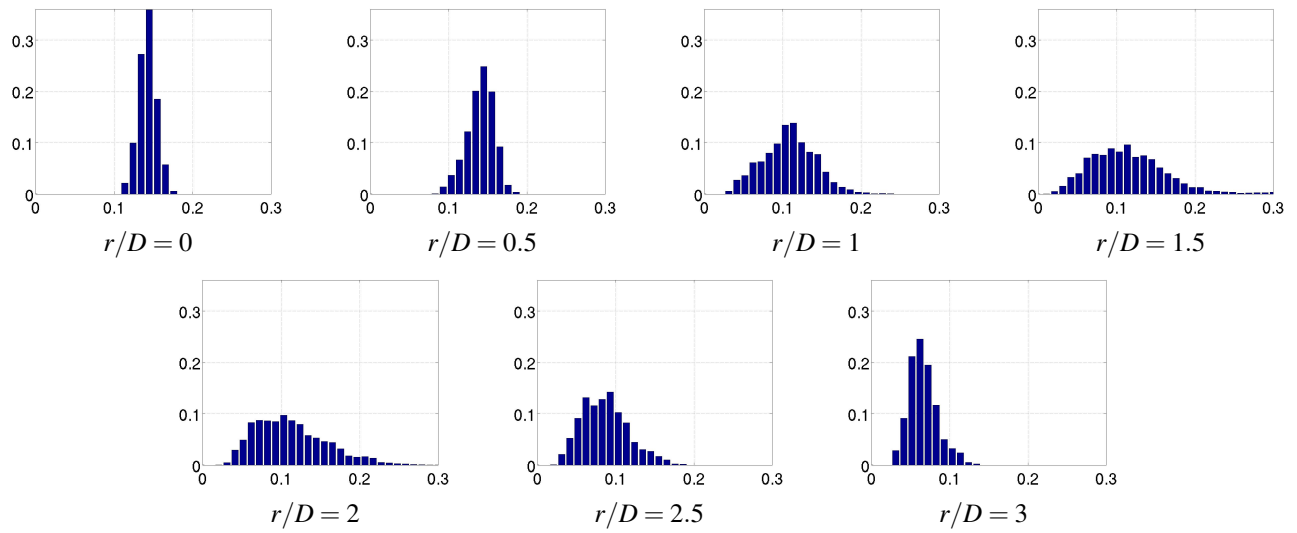


FIGURE 10. Probability density functions of normalized Nusselt number time series at 7 stations along a radius of the configurations obtained with M3.

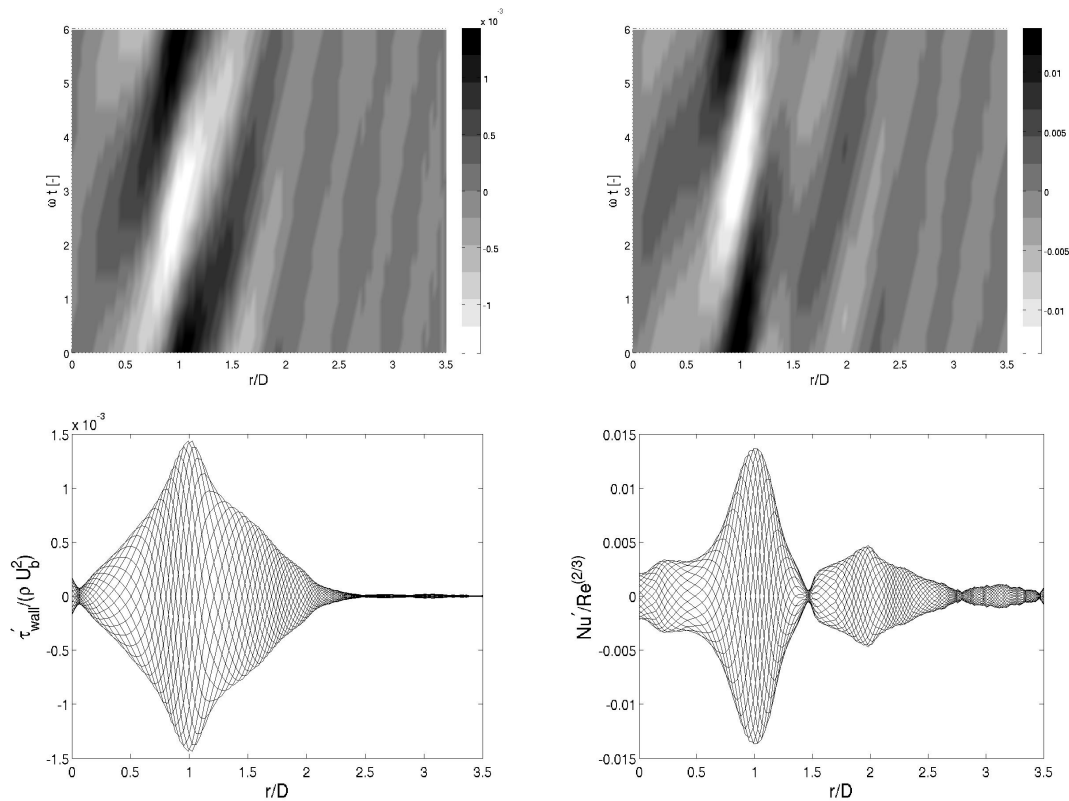


FIGURE 11. One phase expansion of the local power spectral density projection obtained at a Strouhal number $St = 0.63 St_b$ of the temporal simulation along the radius of the jet. Fluctuating friction $(\tau_{wall}^{St})'$ (left) and fluctuating heat flux $(Nu^{St})'$ (right) obtained with M3. Space-time representation (upper) and envelopes along the radial direction (lower).

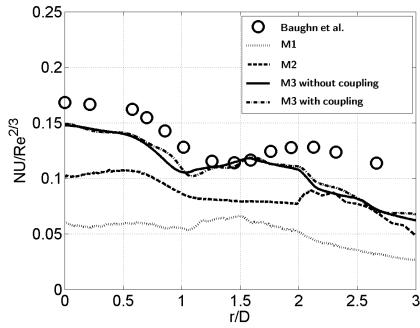


FIGURE 12. Radial distribution of normalized Nusselt number on the impinging wall. The Nusselt number is normalized as proposed in [14].

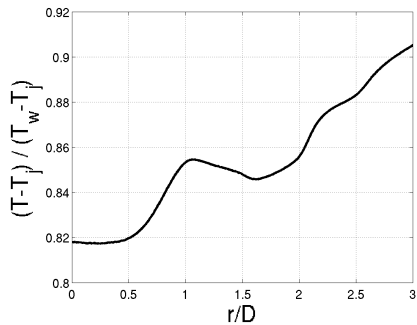


FIGURE 13. Radial temperature distribution at the fluid/solid interface in the CHT case.

$h(r) = q_w(r)/(T_w(r) - T_j)$, q_w being the wall heat flux, depends only on the aerodynamics. Figure 13 gives the radial distribution of temperature of the fluid/solid interface obtained by the CHT simulation. The temperature profile follows the Nusselt number one, showing lower temperature when convective heat flux increases. The 4 main flow regimes in the near wall region have an important impact on the temperature distribution.

5 Conclusion

Large Eddy Simulation has been coupled with a thermal solver to investigate the flow field and heat transfer in an impinging jet at Reynolds number of 23 000 and nozzle to wall distance of $H/D = 2$. The analysis of the flow field gives a comprehensive view of the main flow unsteady features responsible for heat transfer, mainly the stagnation flow, the vortex ring formation as well as the development of the turbulent wall jet. The meshing strategy (hybrid grid with 5 layers of prisms at the wall and tetrahedra elsewhere) combined with a high fidelity LES solver gives accurate predictions of the global mean aerodynamic quantities. Due to the combination of mesh resolution, numerical scheme

and sub-grid scale model, the simulations overestimate the fluctuating quantities in the shear layer regions. Mesh convergence underlines the known result that wall-resolved LES requires discretisations for which y^+ is of the order of one. Due to the mesh size constraint, this target is not obtained in this study, the y^+ of the finer grid resolution being around 5. The impacts on wall heat transfer are direct: the global tendency of the Nusselt number distribution are well captured, nevertheless, the location of the second pick is altered in the simulation and underestimations of heat fluxes are observed. Four main regions have been identified in the fluid wall interaction: (1) the impact region, (2) the development of a laminar pulsed boundary layer due to vortex ring convection, (3) the transition of the boundary layer toward turbulence due to vortex interactions and (4) the development of the turbulent boundary layer. Original post-treatment as space-time plots, probability density function of time series, power spectral density analyses are proposed to investigate the role of unsteady flow structures on heat transfer in these regions. Deeper analyzes have to be done in this direction to give clear insights on interactions between mesh resolution, numerical scheme and sub-grid scale model on the wall heat transfer predictions. Finally, it was shown that the heat flux obtained by the isothermal computation and by the coupled one are very similar all along the wall which can be important for designers to extract a unique convective coefficient for a given flow configuration.

REFERENCES

- [1] Lakshminarayana, B., 1996. *Fluid Dynamics and Heat Transfer of Turbomachinery*. Wiley.
- [2] Lefebvre, A. H., 1999. *Gas Turbines Combustion*. Taylor & Francis.
- [3] Schiele, R., and Wittig, S., 2000. “Gas turbine heat transfer: Past and future challenges”. *J. Prop. Power*, **16**(4), July, pp. 583–589.
- [4] Bunker, R. S., 2006. “Gas turbine heat transfer: 10 remaining hot gas path challenges”. In *Proceedings of GT2006*. ASME Turbo Expo 2006.
- [5] He, L., 2013. “Fourier spectral method for multi-scale aerothermal analysis”. *International Journal of Computational Fluid Dynamics*, **27**(2), pp. 118–129.
- [6] Gardon, R., and Akfirat, J., 1965. “The role of turbulence in determining the heat transfer characteristics of impinging jets”. *Int. J. Heat and Mass Transfer*, **8**(10), pp. 1261–1272.
- [7] Hoogendoorn, C., 1977. “The effect of turbulence on heat transfer at a stagnation point”. *Int. J. Heat and Mass Transfer*, **20**(12), pp. 1333–1338.
- [8] Jambunathan, K., Lai, E., Moss, M., and Button, B., 1992. “A review of heat transfer data for single circular jet impingement”. *Int. J. Heat Fluid Flow*, **13**(2), pp. 106–115.

- [9] L. Geers, M. Tummers, K. H., 2004. “Experimental investigation of impinging jet arrays”. *Exp. Fluids*, **36**, p. 946.
- [10] Hadziabdic, M., and Hanjalic, K., 2008. “Vortical structures and heat transfer in a round impinging jet”. *J. Fluid Mech.*, **596**, pp. 221–260.
- [11] Lodato, G., Vervisch, L., and Domingo, P., 2009. “A compressible wall-adapting similarity mixed model for large-eddy simulation of the impinging round jet”. *Phys. Fluids*, **21**(3), March, p. 035102.
- [12] Tummers, M. J., Jacobse, J., and Voorbrood, S. G., 2011. “Turbulent flow in the near field of a round impinging jet”. *International Journal of Heat and Mass Transfer*, **54**, pp. 4939–4948.
- [13] Weigand, B., and Spring, S., 2011. “Multiple jet impingement – a review”. *Heat Transfer Res.*, **42**(2), pp. 101–142.
- [14] Uddin, N., Neumann, S., and Weigand, B., 2013. “LES simulations of an impinging jet: On the origin of the second peak in the Nusselt number distribution”. *International Journal of Heat and Mass Transfer*, **57**, pp. 356–368.
- [15] Bhaskaran, R., and Lele, S. K., 2010. “Large eddy simulation of free-stream turbulence effects on heat transfer to a high-pressure turbine cascade”. *Journal of Turbulence*, p. N6.
- [16] Duchaine, F., Maheu, N., Moureau, V., Balarac, G., and Moreau, S., 2013. “Large eddy simulation and conjugate heat transfer around a low-mach turbine blade”. In ASME Turbo Expo, GT2013-94257, ed.
- [17] Piacentini, A., Morel, T., Thevenin, A., and Duchaine, F., 2011. “Open-palm: an open source dynamic parallel coupler”. In IV International Conference on Computational Methods for Coupled Problems in Science and Engineering.
- [18] Duchaine, F., Jauré, S., Poitou, D., Quémerais, E., Staffelbach, G., Morel, T., and Gicquel, L., 2013. “High performance conjugate heat transfer with the openpalm coupler”. In V International Conference on Computational Methods for Coupled Problems in Science and Engineering.
- [19] Poinso, T., and Veynante, D., 2005. *Theoretical and Numerical Combustion*. R.T. Edwards, 2nd edition.
- [20] Sagaut, P., 2000. *Large Eddy Simulation for incompressible flows*. Scientific computation series. Springer-Verlag.
- [21] Ferziger, J. H., and Perić, M., 1997. *Computational Methods for Fluid Dynamics*. Springer Verlag, Berlin, Heidelberg, New York.
- [22] Smagorinsky, J., 1963. “General circulation experiments with the primitive equations: 1. the basic experiment”. *Mon. Weather Rev.*, **91**, pp. 99–164.
- [23] Pope, S. B., 2000. *Turbulent flows*. Cambridge University Press.
- [24] Nicoud, F., and Ducros, F., 1999. “Subgrid-scale stress modelling based on the square of the velocity gradient”. *Flow, Turb. and Combustion*, **62**(3), pp. 183–200.
- [25] Schönfeld, T., and Rudgyard, M., 1999. “Steady and unsteady flows simulations using the hybrid flow solver avbp”. *AIAA Journal*, **37**(11), pp. 1378–1385.
- [26] Selmin, V., 1987. Third-order finite element schemes for the solution of hyperbolic problems. Tech. Rep. 707, INRIA report.
- [27] Colin, O., and Rudgyard, M., 2000. “Development of high-order Taylor-galerkin schemes for unsteady calculations”. *J. Comput. Phys.*, **162**(2), pp. 338–371.
- [28] Donea, J., and Huerta, A., 2003. *Finite Element Methods for Flow Problems*. John Wiley & Sons Inc, New York.
- [29] Staffelbach, G., Gicquel, L., Boudier, G., and Poinso, T., 2009. “Large eddy simulation of self-excited azimuthal modes in annular combustors”. *Proc. Combust. Inst.*, **32**, pp. 2909–2916.
- [30] Gicquel, L., Staffelbach, G., and Poinso, T., 2012. “Large eddy simulations of gaseous flames in gas turbine combustion chambers”. *Progress in Energy and Combustion Science*, **38**(6), pp. 782–817.
- [31] Collado Morata, E., Gourdain, N., Duchaine, F., and Gicquel, L. Y. M., 2012. “Effects of free-stream turbulence on high pressure turbine blade heat transfer predicted by structured and unstructured LES”. *International Journal of Heat and Mass Transfer*, **55**(21-22), Oct., pp. 5754–5768.
- [32] Boileau, M., Duchaine, F., Jouhaud, J.-C., and Sommerer, Y., 2013. “Large eddy simulation of heat transfer around a square cylinder using unstructured grids”. *AIAA Journal*, **51**(2), pp. 372–385.
- [33] Frayssé, V., Giraud, L., Gratton, S., and Langou, J., 2005. “A set of GMRES routines for real and complex arithmetics on high performance computers”. *ACM Trans. Math. Softw.*, **31**(2), pp. 228–238.
- [34] Cooper, D., Jackson, D., Launder, B., and Liao, G., 1993. “Impinging jet studies for turbulence model assessment”. *International Journal of Heat and Mass Transfer*, **36**, p. 2675.
- [35] Poinso, T., and Lele, S., 1992. “Boundary conditions for direct simulations of compressible viscous flows”. *J. Comput. Phys.*, **101**(1), pp. 104–129.
- [36] Guezennec, N., and Poinso, T., 2009. “Acoustically non-reflecting and reflecting boundary conditions for vorticity injection in compressible solvers”. *AIAA Journal*, **47**, pp. 1709–1722.
- [37] Granet, V., Vermorel, O., Leonard, T., Gicquel, L., and Poinso, T., 2010. “Comparison of nonreflecting outlet boundary conditions for compressible solvers on unstructured grids”. *AIAA Journal*, **48**(10), pp. 2348–2364.
- [38] Dubief, Y., and Delcayre, F., 2000. “On coherent-vortex identification in turbulence”. *J. Turb.*, **1**, pp. 1–22.
- [39] Baughn, J., and Shimizu, S., 1989. “Heat transfer measurements from a surface with uniform heat flux and an impinging jet”. *J. Heat Transfer*, **111**, pp. 1096–1098.